Industrial Crops & Products 246 (2026) 123382

Contents lists available at ScienceDirect

Industrial Crops & Products

journal homepage: www.elsevier.com/locate/indcrop

Structure-tailored hierarchical porous biochar from banana straw: Pore evolution and formation mechanisms

Chengxiang Gao [a,1], Yangzhi Liu [a,1], Yuxue Liu [a], Hanjing Xu [b], Lidan Zhang [b], Junwei Ma [a,*], Xiaolin Fan [b,*]

[a] State Key Laboratory for Quality and Safety of Agro-Products, Zhejiang Provincial Key Laboratory of Agricultural Microbiomics, Institute of Environment, Resource, Soil and Fertilizer, Zhejiang Academy of Agricultural Sciences, Hangzhou 310021, China
[b] Guangdong Engineering Technology Research Center of Green Inputs for Low-carbon Agriculture, South China Agricultural University, Guangzhou City 510642, China

ARTICLE INFO

Keywords:
Banana straw
Biochar
Pore evolution
Pore structure
Industrial crop residues

ABSTRACT

A well-developed pore structure is essential for the application of biochar in agricultural and environmental fields, and its formation is largely determined by pyrolysis conditions and intrinsic feedstock properties. In this study, banana straw biochar (BSBC) was selected as a representative herbaceous biochar to investigate pore formation mechanisms during pyrolysis. The results show that pore evolution follows a four-stage transition from "biological inheritance" to "thermochemical reconstruction," in which I pores are morphology-retaining structures inherited from plant tissues and organs; II pores are multilayer structures formed within stomata under high-temperature pyrolysis; III pores are hemispherical surface features locally induced by moderate KOH activation; and IV pores are interconnected networks generated through the synergistic effects of high pyrolysis temperature and intensive KOH activation. Pore density increases progressively from Pore I to Pore IV, while circularity reaches a minimum in Pore II and a maximum in Pore III. Further analysis indicates that endogenous elements in the raw material play a significant regulatory role in pore evolution. Specifically, Si acts as a structural stabilizing factor that partially suppresses the collapse of the carbon framework, whereas K promotes pore formation and development by catalyzing carbon structural rearrangement and etching reactions. With increasing thermochemical severity, the specific surface area of biochar increases markedly from 7.72 $m^2 \cdot g^{-1}$ to 962.09 $m^2 \cdot g^{-1}$, indicating a transformation from natural biological structures to high-surface-area porous functional materials, in which micropores dominate the overall surface area contribution. This study provides a structural evolution framework and theoretical basis for the rational design of hierarchically porous biochars derived from agricultural residues.

1. Introduction

Banana (*Musa* spp.) is one of the most important fruit crops worldwide and plays a critical role in agricultural production, food supply, and rural economies in tropical and subtropical regions (FAO., 2025). However, banana production is severely threatened by Fusarium wilt, a destructive soil-borne disease caused by *Fusarium oxysporum* f. sp. *cubense* Tropical Race 4 (Foc TR4). Infected banana plants generate large amounts of diseased straw, which can act as a persistent source of pathogen inoculum if not properly managed (Zhang et al., 2025; Li et al., 2022; Murali et al., 2021). Conventional disposal methods, such as open burning or landfilling, are insufficient to eliminate disease transmission risks and may lead to secondary environmental pollution (Gao et al., 2024). Therefore, the development of safe and effective strategies for the treatment and valorization of diseased banana straw is essential for the long-term sustainability of the banana industry.

Thermal conversion of biomass into biochar is widely recognized as a promising approach for the safe treatment and value-added utilization of agricultural residues (Fei et al., 2026; Jing et al., 2026; Mandal et al., 2026). High-temperature pyrolysis can effectively inactivate plant pathogens, while the resulting biochar has demonstrated multifunctional applications in agricultural and environmental systems (Rana et al., 2025; Wang et al., 2025a). Previous studies have shown that porous biochar derived from diseased banana straw not only mitigates

---

* Corresponding authors.
E-mail addresses: majw@zaas.ac.cn (J. Ma), xlfan@scau.edu.cn (X. Fan).
[1] Co-first author; Both authors have equally contributed

https://doi.org/10.1016/j.indcrop.2026.123382
Received 2 February 2026; Received in revised form 26 April 2026; Accepted 29 April 2026

pathogenic risks but also exhibits strong adsorption capacity for heavy metals, such as cadmium, in aqueous environments (Gao et al., 2024). These findings highlight the potential of banana straw biochar as a multifunctional material for addressing both agricultural residue management and environmental remediation challenges. The multifunctional performance of biochar is closely linked to its pore architecture, which governs mass transfer, adsorption behavior, and surface reactivity. In particular, complex pore structures often facilitate enhanced interactions between biochar and contaminants or nutrients. Although banana straw-derived biochar has been reported to exhibit well-developed porosity, the formation and evolution of its pore architecture during thermal conversion and chemical modification remain poorly understood. This lack of mechanistic understanding limits the rational design and broader application of banana straw biochar in agricultural and environmental fields.

Pore formation in biochar is generally governed by both intrinsic factors, such as the elemental composition and anatomical structure of the feedstock, and extrinsic factors, including pyrolysis temperature and chemical activation conditions. Intrinsic factors primarily involve the inherent chemical composition of the feedstock, such as organic acid salts and specific carbon precursors (Mian et al., 2023; Cheng et al., 2019; He et al., 2019; Zhao et al., 2019a). Certain naturally occurring components can function as self-activating agents, thereby promoting pore formation. For example, Niu et al. (2017) reported that carbon dioxide released from hydroxyapatite in bovine bone at high temperatures facilitated the formation of porous biochar. Similarly, Chen et al. (2012) demonstrated that the high potassium content in pokeweed acted as a self-activator, enhancing pore development through the volatilization and release of potassium species during pyrolysis. Zeng et al. (2018) further observed the formation of circular pores in water hyacinth biochar, which was attributed to the escape of potassium vapor from the carbon skeleton. In contrast, extrinsic factors mainly involve biochar preparation conditions, among which pyrolysis temperature and chemical activating agents play dominant roles in pore development. Bonelli et al. (2007) reported that the surface area and porosity of biochar increased with increasing pyrolysis temperature, accompanied by the gradual degradation of cellulose and lignin and the formation of vascular bundle-like channel structures. In addition, pore-blocking substances and volatile gases generated during pyrolysis can be removed at elevated temperatures, thereby creating additional pore space (Fang et al., 2023; Rafiq et al., 2016; Shaaban et al., 2014). Chemical modification of feedstock using exogenous agents, such as acids, alkalis, and metal salts, is also recognized as a major extrinsic factor influencing pore development. Activating agents including NaOH, KOH, H_3PO_4, and $KMnO_4$ have been widely applied to biochar production at both laboratory and industrial scales (Mustafa et al., 2026; Qiu et al., 2019; Zhang et al., 2019; Brito et al., 2018). For instance, Herath et al. (2021) obtained porous wood biochar with a high specific surface area of 1049 $m^2 \cdot g^{-1}$ by KOH activation of Douglas fir green wood chips, while Peng et al. (2017) produced pine sawdust biochar with a surface area of 900 $m^2 \cdot g^{-1}$ using H_3PO_4 modification. However, existing studies have predominantly focused on the effects of individual extrinsic parameters, particularly pyrolysis temperature or activating agents, whereas the roles of intrinsic feedstock characteristics have received comparatively limited attention. Moreover, most investigations have centered on woody biomass or major field crop residues, while herbaceous residues from industrial fruit crops, such as banana straw, remain underexplored. This research bias may lead to an incomplete understanding of pore evolution mechanisms in biochar derived from herbaceous biomass.

In this study, banana straw was selected as a representative herbaceous industrial crop residue to systematically investigate the coupled effects of intrinsic feedstock characteristics and thermal-chemical perturbations on biochar pore evolution. By integrating SEM-EDS observations with BET analysis, the pore structures of banana straw biochar produced under varying pyrolysis temperatures and KOH impregnation conditions were classified based on morphological features, and their evolutionary pathways were examined. By elucidating the mechanisms underlying pore formation and structural evolution, this work provides a theoretical basis for the controlled design of banana straw biochar (BSBC) and broadens its potential applications in agricultural and environmental systems.

2. Materials and methods

2.1. Feedstocks and reagents

Feedstocks, including banana, rice, and maize straw, were collected separately from the research station of the Guangdong Provincial Engineering Technology Research Center of Low-Carbon Agriculture and Green Inputs, South China Agricultural University (SCAU). All feedstocks complied with relevant institutional, national, and international guidelines and legislation, as well as the IUCN Policy Statement on Research Involving Species at Risk of Extinction and the Convention on International Trade in Endangered Species of Wild Fauna and Flora (CITES). The collected feedstocks were washed with tap water, oven-dried at 105 °C to constant weight, and then crushed to pass through a 2 cm sieve. This particle size was selected to retain the original structural features of the feedstocks, facilitating subsequent impregnation and morphological observation. Potassium hydroxide (KOH, 90% purity) was an industrial-grade reagent purchased from Fuchen (Guangzhou) Chemical Reagents Co., Ltd.

2.2. Preparation of biochar from different raw material

The carbon materials prepared in this study were modified biochars rather than commercial activated carbon. The crushed banana, rice, and maize straw samples were separately pyrolyzed using a programmable tubular carbonization reactor (TF12P100, Tianjin Taisite Instrument Co., Ltd., China). Pyrolysis was conducted by heating the feedstocks at a rate of 3 $°C \cdot min^{-1}$ to 800 °C and maintaining this temperature for 2 h under controlled conditions. After cooling the reactor naturally to room temperature, the resulting biochars were collected and denoted as $BSBC_{800}$, $RSBC_{800}$, and $MSBC_{800}$ for banana straw biochar, rice straw biochar, and maize straw biochar, respectively.

2.3. Preparation of biochar from different pyrolysis temperature and KOH impregnation

Potassium hydroxide (KOH) was selected as the chemical modifying agent for banana straw biochar to promote pore development, based on preliminary screening experiments (see Section 3.4 for details). Banana straw was impregnated with 0.5 M and 1.5 M KOH solutions for 2 h, respectively. After impregnation, the samples were oven-dried at 105 °C to constant weight. The dried banana straw was then pyrolyzed at 500 °C or 800 °C for 2 h. The resulting biochars were designated as $BSBC_{0.5M\text{-}KOH\text{-}500}$, $BSBC_{1.5M\text{-}KOH\text{-}500}$, $BSBC_{0.5M\text{-}KOH\text{-}800}$, and $BSBC_{1.5M\text{-}KOH\text{-}800}$, respectively.

2.4. Characterization of pore morphology of biochar

The dried biochar samples and their corresponding feedstocks were sputter-coated with a gold layer (~2 nm thickness) using a Polaron sputter coater, with the coating process repeated four times to ensure adequate conductivity. The pore morphology and elemental composition of the samples were subsequently characterized using scanning electron microscopy coupled with energy-dispersive X-ray spectroscopy (SEM–EDS; EVO 10, Carl Zeiss, Germany). According to the experimental design, the SEM was operated at an accelerating voltage of 10 kV with a probe current of 15 mA to obtain stable imaging conditions and reliable elemental analysis.

2.5. *Measurement of textural properties of biochar*

Specific surface area (S_{BET}), average pore diameter (PD) and pore volume (PV) were measured by use of Brunauer-Emmett-Teller (BET) specific surface area analyzer (ASAP 2020, USA). Nitrogen adsorption was selected as the method of analysis, which was widely recognized for its efficacy in characterizing porous materials. The operational temperature was deliberately maintained at 77 K, a standard condition that corresponds to the boiling point of liquid nitrogen and was instrumental in minimizing the effects of thermal motion, thereby enhancing the accuracy of the adsorption measurements. This approach was chosen based on its proven ability to yield reliable and reproducible results, which were critical for the comparative analysis presented in this study. In addition, to quantitatively characterize the pore morphology in SEM images, ImageJ software was used for statistical analysis. Through image thresholding and binarization, pore contour information was extracted, and morphological parameters including pore density, porosity, circularity, and aspect ratio were calculated.

2.6. *Determination of elemental compositions of biochar*

The elemental composition of biochar (Table 1), including carbon (C), hydrogen (H), nitrogen (N), and oxygen (O), was determined using an elemental analyzer (Vario EL cube, Elementar, Germany). Prior to analysis, the biochar samples were finely ground and homogenized to ensure representative and consistent measurements.

2.7. *Data processing*

Raw experimental data were organized and preliminarily processed using Microsoft Excel 2020. Statistical analyses were performed with SPSS Statistics v26.0 (IBM Corp., Armonk, NY, USA). Prior to analysis, data normality and homogeneity of variance were assessed where appropriate. Origin 2024 (OriginLab Corporation, Northampton, MA, USA) was used for plotting Figures.

3. Results

3.1. *Pore morphology of banana straw biochar*

The evolution of biochar pore architecture revealed by SEM–EDS was well supported by BET analysis, together demonstrating a progressive transition from biologically inherited pores to newly developed pores. Based on their morphological characteristics, the pore structures were systematically classified into four categories. Category I pores preserved the original anatomical structures of banana straw. As shown in Fig. 1A and B, the pores highlighted by red circles originated from vessels (A1), veins and intercellular spaces (A2), cellular compartments (B1), and stomata (B2). This category also included pores associated with the epidermis, vascular bundles, and other plant tissues and organs. Category II pores formed as multilayer structures on the internal carbon skeleton within Category I pores and resulted from partial tissue destruction at elevated pyrolysis temperatures. The development of these pores significantly increased mesopore abundance and total pore volume. As illustrated in Fig. 1B, the first-layer (yellow circles) and second-layer pores (green circles) formed on the inner walls of cellular compartments or stomata were classified as Category II pores. At this stage, the biochar largely retained the external morphology of the feedstock, although the internal carbon skeleton was progressively disrupted and replaced by layered pore structures. Category III pores were characterized by hemispherical concavities on the biochar surface (Fig. 1C2), which promoted the development of both mesopores and micropores and led to a marked increase in specific surface area (SSA). Notably, Category I pores were still present at this stage (Fig. 1C1). Category IV pores consisted of interconnected pore networks formed on a newly reorganized carbon skeleton (Fig. 1D). These pores were dominated by micropores and small mesopores, corresponding to the highest SSA and pore volume among all categories. This pore type developed through the combined evolution of the preceding pore categories. At this stage, the biochar completely lost the original morphology of the feedstock (D1) and transformed into a highly perforated porous material (D2). Overall, this classification highlights a continuous transition from inherited biological pores (Fig. 1E) to newly generated pores during pyrolysis and chemical activation, providing a structural framework for understanding biochar pore evolution. The underlying formation mechanisms are further discussed in the following section.

Table 1
Elemental composition results of biochar.

Biochar Samples	C	H	O	N	S	H/C	O/C
$BSBC_{500}$	55.56	1.85	17.32	0.72	0.21	0.40	0.23
$BSBC_{0.5MKOH\text{-}500}$	47.11	1.50	20.94	0.64	0.28	0.38	0.33
$BSBC_{1.5MKOH\text{-}500}$	33.22	1.09	34.67	0.24	0.15	0.39	0.78
$BSBC_{800}$	28.86	1.42	35.74	0.19	0.23	0.59	0.93
$BSBC_{0.5MKOH\text{-}800}$	21.52	1.42	37.60	0.15	0.18	0.79	1.31
$BSBC_{1.5MKOH\text{-}800}$	14.58	1.50	37.20	0.10	0.06	1.24	1.91

Notes: $BSBC_{0.5MKOH\text{-}500}$ and $BSBC_{0.5MKOH\text{-}800}$ refer to the biochars obtained by pyrolysis of banana straw (impregnated in 0.5 M KOH solution) at 500 °C and 800 °C, respectively. $BSBC_{1.5MKOH\text{-}500}$ and $BSBC_{1.5MKOH\text{-}800}$ refer to the biochars obtained by pyrolysis of banana straw (impregnated in 1.5 M KOH solution) at 500 °C and 800 °C, respectively. $BSBC_{500}$ and $BSBC_{800}$ refer to the biochars obtained by pyrolysis of banana straw at 500 °C and 800 °C, respectively.

3.2. *Formation of category I and II pores*

As shown in Fig. 1A and B, Category I pores (red circles) exhibited non-proportional shrinkage while largely retaining the original morphology of the feedstock tissues and organs. This shrinkage was associated with the volatilization of bound water and thermally unstable components in banana tissues during pyrolysis, leading to mass loss and overall volume reduction in the biochar. However, the extent of shrinkage varied among different tissues and organs due to their heterogeneous contents of bound water and unstable components. Following the volatilization of these components, the middle lamella of the cell wall disappeared, resulting in a denser pore structure and a more clearly defined carbon skeleton. Notably, this pore morphology mainly reflects the intrinsic anatomical characteristics of banana straw and represents an early-stage pore structure formed under relatively mild thermal conditions.

The development of Category II pores was influenced by both the intrinsic composition of the feedstock and the pyrolysis temperature. As shown in Fig. 1B, Category II pores (yellow and green circles) appeared as multilayer pore structures formed within Category I pores (red circles). Specifically, Category I pores constituted the outermost layer, while the pores indicated by the yellow circles represented the second layer formed within the carbon skeleton of the first-layer pores. Subsequently, third-layer pores (green circles) developed within the second-layer pores, resulting in a hierarchical, layer-by-layer pore architecture. Notably, Category II pores were not observed in maize or rice straw biochars. As shown in Fig. 2A1, 2B1, and 2C1, similar stomatal structures (blue circles) were present in the raw banana, maize, and rice straws, although more granular materials were attached around the stomata in rice straw. After pyrolysis at 800 °C, the stomatal structure of banana straw biochar exhibited pronounced morphological changes compared with the raw material. The stomata not only lost their original shape but also developed distinct multilayer pore structures (Fig. 2A2). In contrast, the stomatal morphology of maize and rice straw biochars (Fig. 2B2 and 2C2) remained largely similar to that of their respective feedstocks, with minimal changes in size and shape. Overall, the formation of this pore type was closely associated with the thermal decomposition behavior of banana straw, indicating that its inherent elemental composition was more favorable for the development of

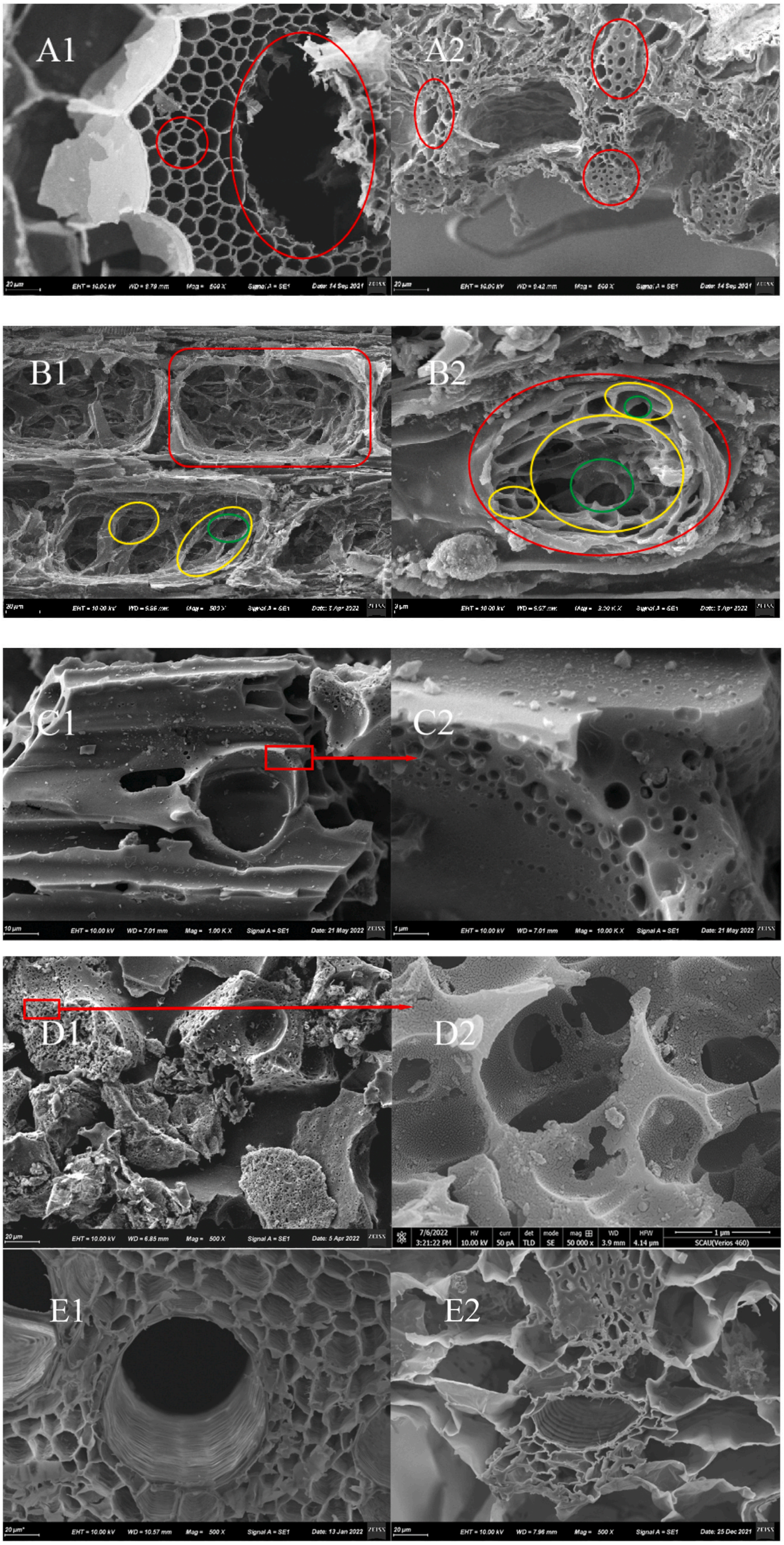

Fig. 1. Four pore categories of banana straw biochar. Notes: The red circles in A and B refer to Category I pores. The yellow and green circles in B refer to Category I and second layers of the Category II pores, respectively. C and D refer to the Category III and IV pores, respectively. E refer to the pores of banana straw.

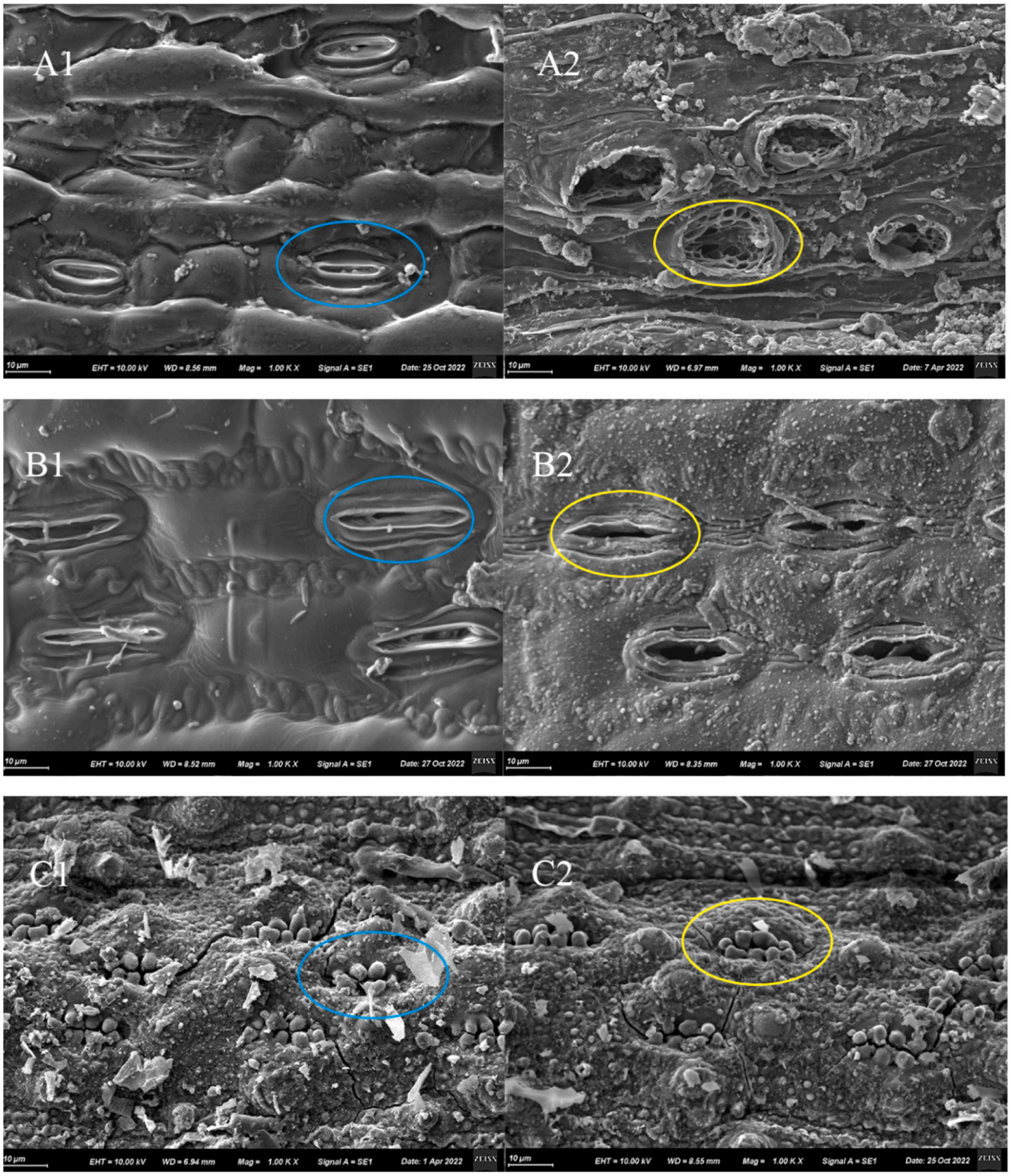

Fig. 2. SEM images of the stoma of Banana straw (A1), Maize straw (B1), Rice straw (C1) and their biochars of $BSBC_{800}$ (A2), $MSBC_{800}$ (B2) and $RSBC_{800}$ (C2). Notes: $BSBC_{800}$, $MSBC_{800}$ and $RSBC_{800}$ refer to the biochar obtained by pyrolysis of banana, maize and rice straw at 800 °C, respectively.

multilayer pore structures.

To further elucidate the influence of intrinsic feedstock composition on the development of Category II pores, the elemental compositions of banana straw, maize straw, rice straw, and their corresponding biochars were analyzed by SEM-EDS. The results indicated that the contents of C, Si, and K in the feedstocks were closely associated with the formation of Category II pores. Compared with maize and rice straw (Table 2), banana straw exhibited the highest C content (71.61%) and the lowest Si (1.95%) and K (1.90%) contents. This compositional pattern was largely preserved after carbonization. Specifically, the C content of banana straw biochar (55.38%) remained higher than that of maize (28.58%) and rice straw biochars (13.08%), whereas its Si (6.27%) and K (5.29%) contents were markedly lower than those of maize straw biochar (21.30% and 10.89%) and rice straw biochar (31.71% and 15.99%). These results further demonstrate that the development of Category II pores is strongly dependent on the intrinsic elemental composition of the feedstock.

On the one hand, SEM-EDS analysis shows that the silicon content in banana straw is only 34.88% and 12.24% of that in corn and rice straw, respectively, and its biochar silicon content is also only 29.43% and 19.77% of the latter two (Table 2), indicating that corn and rice straw retain a higher proportion of silicon under the same pyrolysis conditions. Previous studies have reported that silicon, as a thermally stable element, can protect the carbon framework during pyrolysis (Koyama and Hayashi, 2017). Rice husk biochar, in particular, is rich in silicon,

Table 2
EDS results of the stoma of banana straw, maize straw, rice straw and their biochar from $BSBC_{800}$, $MSBC_{800}$, and $RSBC_{800}$.

Sample	C content (%)	O content (%)	Si content (%)	K content (%)
Banana straw	71.61	23.93	1.95	1.9
Maize straw	50.2	41.48	5.59	2.28
Rice straw	47.17	33.67	15.92	2.85
$BSBC_{800}$	55.38	22.2	6.27	5.29
$MSBC_{800}$	28.58	37.48	21.3	10.89
$RSBC_{800}$	13.08	38.8	31.71	15.99

Notes: $BSBC_{800}$, $MSBC_{800}$ and $RSBC_{800}$ refer to the biochar obtained by pyrolysis of banana, maize and rice straw at 800 °C, respectively.

and its thermal stability is closely related to the protective effect of Si-C structures in the feedstock (Guo and Chen, 2014; Xiao et al., 2014). Subsequent studies further confirmed that higher silicon content enhances biochar stability (Liu et al., 2020; Zhao et al., 2019b). This is because Si is mainly converted into thermally stable amorphous $SiO2$ during pyrolysis. This inorganic phase exhibits high thermal stability and chemical inertness, which helps stabilize the carbon framework during carbonization (Zheng et al., 2024). Therefore, the relatively low silicon content in banana straw implies weaker protection of the carbon skeleton during pyrolysis, which in turn favors the formation of a multilayered pore structure.

On the other hand, the potassium content of all three feedstocks increased significantly after pyrolysis (Table 2), but their potassium enrichment ratios (defined as the ratio of potassium content in biochar to that in the corresponding raw material) differed markedly. The potassium enrichment ratio of banana straw biochar (2.79) is much lower than that of corn straw biochar (4.77) and rice straw biochar (5.61), indicating that banana straw experienced a greater loss of potassium under the same pyrolysis conditions. Previous studies have confirmed that K exhibits strong catalytic activity at high temperatures and can promote local rearrangement of the carbon framework (Tan et al., 2026; Fu et al., 2019; Hunsom and Autthanit, 2013). The mechanism of KOH-induced pore development can be summarized as follows (Gao et al., 2020; Fu et al., 2019; Hunsom and Autthanit, 2013): (i) the carbon framework is etched by KOH through redox reactions; (ii) gaseous products undergo secondary reactions with carbon; and (iii) metallic potassium causes expansion of the carbon lattice. During pyrolysis, KOH decomposes and reacts with carbon to form K_2O, H_2O vapor, and a small amount of H_2. The generated K_2O further reacts with CO_2 to form K_2CO_3. When the temperature exceeds 762 °C, K_2O or K_2CO_3 reacts with carbon to produce potassium vapor and CO gas. The release of potassium vapor and CO leads to surface damage of the biochar, forming hemispherical pits. Meanwhile, metallic potassium intercalates into the carbon lattice, causing deformation of the carbon layers and thereby promoting pore formation. Therefore, the greater loss of potassium during pyrolysis in banana straw indicates a more pronounced pore-forming effect.

Combined with the BET analysis (Table 2), the results show that biochar prepared at 800 °C exhibits significantly higher specific surface area and pore volume than that produced at 500 °C. The increase in micropore surface area (341.32 $m^2 \cdot g^{-1}$) accounts for 82.68% of the total increase in specific surface area (412.8 $m^2 \cdot g^{-1}$). Similarly, the total pore volume, micropore volume, and mesopore volume of BSBC800 are all significantly higher than those of BSBC500, reaching 9.04, 69.5, and 3.59 times those of the latter, respectively. The increase in micropore volume (0.137 $cm^3 \cdot g^{-1}$) accounts for 70.98% of the total pore volume increment (0.193 $cm^3 \cdot g^{-1}$). Overall, despite non-proportional volumetric shrinkage, Category I pores largely retain the morphological characteristics of the original anatomical structures. The intrinsic elemental composition, particularly silicon and potassium, together with high-temperature pyrolysis, jointly promotes the formation of Category II pores and significantly enhances micropore development.

3.3. *Formation of the category III pores*

To promote pore development in banana straw biochar, several chemical modifiers were screened prior to further experiments. Banana straw was impregnated separately with 0.5 M HNO_3, 0.5 M $FeCl_3$, and 0.5 M KOH solutions. To exclude the influence of high-temperature–induced Category II pores, the pyrolysis temperature was fixed at 500 °C. SEM images of the three modified biochars are presented in Fig. 3. Distinct surface pores were observed on the KOH-modified biochar ($BSBC_{0.5MKOH\text{-}500}$; Fig. 3A and B), indicating that KOH impregnation altered the carbon skeleton and induced pore formation. In contrast, the surfaces of $FeCl_3$-modified biochar ($BSBC_{0.5MFeCl_3\text{-}500}$; Fig. 3C and D) and HNO_3-modified biochar ($BSBC_{0.5MHNO_3\text{-}500}$; Fig. 3E and F) remained largely intact, with no observable pore development. These results demonstrate that impregnation with 0.5 M KOH effectively induced the formation of new pores, whereas 0.5 M $FeCl_3$ and HNO_3 showed negligible effects. Accordingly, KOH was selected as the modifying agent for inducing Category III pores.

As reported by Tan et al. (2026), low-concentration KOH is primarily accumulated on the biochar surface and induces pore formation (Effects of intrinsic and external potassium on biochar structure evolution in volatile–char interactions during biomass pyrolysis). SEM observations (Fig. 1C) further confirm that, in addition to Type I pores, hemispherical pores are formed on the biochar surface. BET analysis (Table 3) showed that, compared with $BSBC_{500}$, the specific surface area of $BSBC_{0.5MKOH\text{-}500}$ and $BSBC_{1.5MKOH\text{-}500}$ increased by 281.14 and 564.95 $m^2 \cdot g^{-1}$, respectively. Of these increases, the micropore surface area contributed 249.44 and 496.81 $m^2 \cdot g^{-1}$, accounting for 88.72% and 87.99% of the total surface area increment, respectively. Correspondingly, the pore volume increased by 0.16 and 0.29 $cm^3 \cdot g^{-1}$, while the

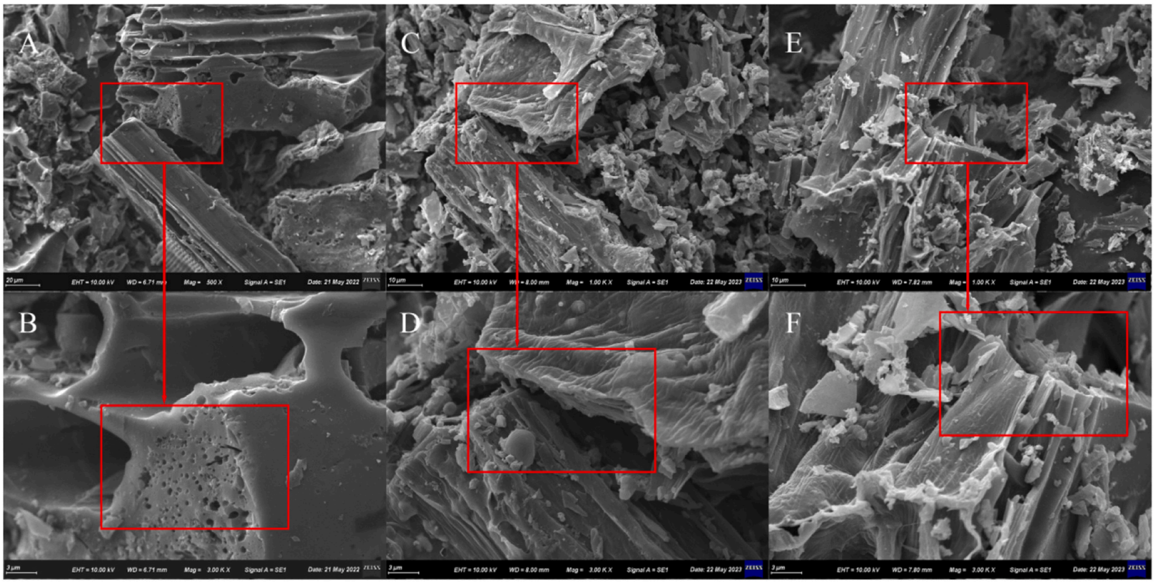

Fig. 3. SEM images of $BSBC_{0.5MKOH\text{-}500}$ (A, B), $BSBC_{0.5MFeCl3\text{-}500}$ (C, D) and $BSBC_{0.5MHNO3\text{-}500}$ (E, F). Notes: $BSBC_{0.5MKOH\text{-}500}$, $BSBC_{0.5MFeCl3\text{-}500}$ and $BSBC_{0.5MHNO3\text{-}500}$ refer to the 0.5 M KOH, 0.5 M $FeCl_3$ and 0.5 M KNO_3 modified banana straw biochar prepared at 500 °C, respectively.

Table 3
BET results of biochar.

Biochar Samples	Specific surface area ($m^2 \cdot g^{-1}$)	Micropore area ($m^2 \cdot g^{-1}$)	External surface area ($m^2 \cdot g^{-1}$)	Pore Volume ($cm^3 \cdot g^{-1}$)	Micropore Volume ($cm^3 \cdot g^{-1}$)	Mesoporous Volume ($cm^3 \cdot g^{-1}$)	Pore Diameter (nm)
$BSBC_{500}$	7.72	4.64	3.08	0.024	0.002	0.022	12.31
$BSBC_{0.5MKOH\text{-}500}$	288.86	254.08	34.78	0.179	0.103	0.076	2.48
$BSBC_{1.5MKOH\text{-}500}$	572.67	501.44	71.23	0.309	0.200	0.108	2.16
$BSBC_{800}$	420.55	345.96	74.59	0.217	0.139	0.079	2.07
$BSBC_{0.5MKOH\text{-}800}$	627.68	510.54	117.14	0.335	0.206	0.129	2.13
$BSBC_{1.5MKOH\text{-}800}$	962.09	737.04	225.05	0.524	0.302	0.222	2.18

Notes: $BSBC_{0.5MKOH\text{-}500}$ and $BSBC_{0.5MKOH\text{-}800}$ refer to the biochars obtained by pyrolysis of banana straw (impregnated in 0.5 M KOH solution) at 500 °C and 800 °C, respectively. $BSBC_{1.5MKOH\text{-}500}$ and $BSBC_{1.5MKOH\text{-}800}$ refer to the biochars obtained by pyrolysis of banana straw (impregnated in 1.5 M KOH solution) at 500 °C and 800 °C, respectively. $BSBC_{500}$ and $BSBC_{800}$ refer to the biochars obtained by pyrolysis of banana straw at 500 °C and 800 °C, respectively.

micropore volume increased by 0.10 and 0.20 $cm^3 \cdot g^{-1}$, accounting for 66.45% and 70.18% of the total pore volume increase. Similarly, the specific surface area (627.68 $m^2 \cdot g^{-1}$) and pore volume (0.335 $cm^3 \cdot g^{-1}$) of $BSBC_{0.5MKOH\text{-}800}$ were 1.49 and 1.54 times higher than those of $BSBC_{800}$, respectively. The increase in micropore surface area (164.58 $m^2 \cdot g^{-1}$) accounted for 79.46% of the total surface area increase (207.13 $m^2 \cdot g^{-1}$), while the increase in micropore volume (0.067 $cm^3 \cdot g^{-1}$) contributed 57.26% of the total pore volume increase (0.12 $cm^3 \cdot g^{-1}$). SEM observations (Fig. 1C) further confirmed that, in addition to Category I pores, hemispherical surface pores were formed on the biochar. These results indicate that KOH modification effectively induced the formation of Category III pores in BSBC, and that both the specific surface area and pore volume increased with increasing KOH concentration.

3.4. Formation of the category IV pores

Category IV represents an intensified pore architecture that evolves from previously identified pore types under strong chemical activation conditions. With increasing KOH impregnation concentration, the carbon skeleton of banana straw biochar undergoes pronounced etching and expansion, resulting in the formation of interconnected micro-mesoporous networks accompanied by partial pore wall collapse. BET analysis indicated that at 500 °C, increasing the KOH concentration from 0 to 1.5 M led to a substantial rise in the specific surface area from 7.72 to 572.67 $m^2 \cdot g^{-1}$, accompanied by an increase in pore volume from 0.024 to 0.309 $cm^3 \cdot g^{-1}$. At 800 °C, under the same concentration range, the specific surface area further increased from 420.55 to 962.09 $m^2 \cdot g^{-1}$, while the pore volume expanded from 0.217 to 0.524 $cm^3 \cdot g^{-1}$. Further examination of the microporous structure revealed that both micropore surface area and micropore volume increased with rising KOH concentration at both temperatures, with a more pronounced enhancement observed at 800 °C. These results suggest that the activating effect of KOH on pore development is significantly intensified at higher temperatures, indicating a strong interaction between temperature and KOH concentration in regulating pore structure parameters. In other words, temperature and KOH concentration do not act independently during pore formation; rather, they synergistically enhance the etching and reconstruction of the carbon framework, thereby jointly promoting the development of a Category IV pore structure.

SEM observations (Fig. 1D) showed that the biochar completely lost the morphological features of the original feedstock and transformed into a highly perforated material. The pore morphology evolved from multilayer and hemispherical pores to an interconnected pore network. The N_2 adsorption-desorption isotherms further demonstrate the formation characteristics of a hierarchically interconnected pore network. As shown in the Fig. 4, Category I pores exhibit relatively low adsorption capacity over the entire relative pressure range, with almost no evident hysteresis loop, indicating a predominance of microporous structures with strong pore independence and limited connectivity. This feature is consistent with the preserved anatomical structure of the original biomass. In contrast, Category II, III, and IV pores display typical I/IV hybrid isotherm characteristics, accompanied by varying degrees of hysteresis loops in the medium-to-high pressure region ($P/P_0 > 0.4$), suggesting the development of a certain proportion of mesoporous and microporous structures. Further comparison reveals that, as the pore structure evolves from Category II to Category IV, the area of the hysteresis loop gradually increases, while the adsorption uptake in the high relative pressure region ($P/P_0 \rightarrow 1$) becomes more pronounced. This indicates that capillary condensation is significantly enhanced in Category IV pores, leading to the formation of a more complex hierarchical pore system.

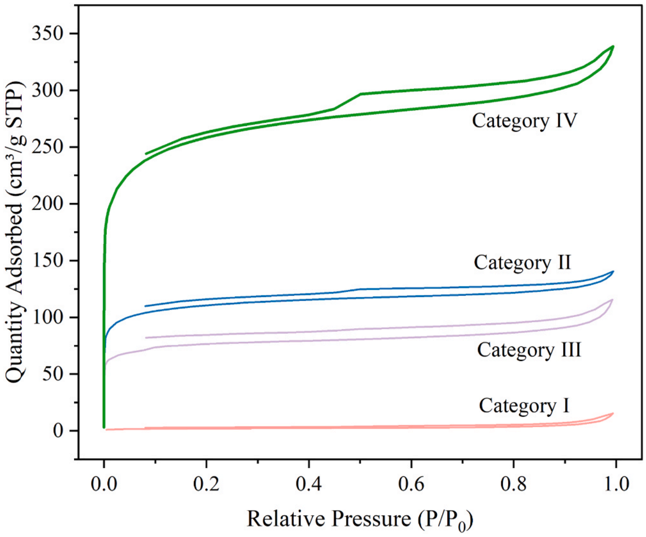

Fig. 4. Nitrogen adsorption-desorption isotherms of the four pore categories.

These results demonstrate that simultaneous increases in pyrolysis temperature and KOH concentration are effective in promoting pore development and inducing the formation of Category IV pores. This transformation is attributed to the combined effects of extensive loss of cellular constituents and severe disruption of the carbon skeleton induced by KOH impregnation, which are further intensified at high pyrolysis temperatures. The volatilization of unstable components leads to collapse and reorganization of the carbon framework, while continuous etching by reactive gaseous species, including potassium vapor, carbon monoxide, and water vapor, facilitates the formation of interconnected pores. Importantly, Category IV pores do not represent a simple amplification of pore quantity generated in earlier stages, but rather a qualitative structural transition involving carbon skeleton collapse and reassembly. This process results in a pore network dominated by micropores and small mesopores, highlighting the synergistic role of high-temperature pyrolysis and intensive KOH activation in driving the transformation of Category I-III pores into Category IV pores. However, although higher KOH concentrations and elevated pyrolysis temperatures resulted in maximum specific surface area and pore volume, their practical applicability should be evaluated in terms of chemical consumption and process cost. From an industrial perspective, moderate KOH impregnation combined with high-temperature pyrolysis may offer a more feasible balance, enabling substantial pore development while limiting chemical input. The pore classification framework proposed in this study provides a useful basis for balancing porosity enhancement and process practicality in the production of biochar from industrial crop residues.

4. Discussion

Banana Fusarium wilt is widely recognized as one of the most destructive diseases affecting global banana production, posing persistent and severe threats to the sustainability of the banana industry (Herrera et al., 2023; Acuna et al., 2022; Maymon et al., 2020; Stokstad, 2019). The disease is characterized by high infectivity, long-term persistence, and difficulty of control. Once established in the field, it is often resistant to conventional agronomic and chemical management practices (Chen et al., 2024; Dehkhoda et al., 2016; Gan et al., 2015). These challenges do not arise from a single cause but result from the combined effects of pathogen biological characteristics, cultivation systems, and soil environmental conditions. Foc TR4 is a typical soil-borne pathogen capable of surviving in soil for prolonged periods, even in the absence of host plants, with reported survival times exceeding 20 years (Gao et al., 2020). In addition, Foc TR4 can persist in asymptomatic alternative hosts (Sing et al., 1985), limiting the effectiveness of crop rotation or fallow strategies. As a vascular-invading pathogen, once Foc TR4 colonizes plant tissues, it can largely evade non-systemic fungicides and non-endophytic biocontrol agents, thereby substantially reducing the efficacy of field-level disease control (Wang et al., 2024). Moreover, the pathogen spreads through multiple pathways, including infected planting materials, contaminated soil carried by farm workers and machinery, and irrigation water (Cheng et al., 2019). Long-term monoculture of banana, particularly the large-scale continuous cultivation of Cavendish cultivars, creates a highly homogeneous host environment that facilitates the establishment and spread of Foc TR4 (Chen et al., 2024; Yu et al., 2018). Concurrently, soil acidification further enhances pathogen adaptability and increases the likelihood of disease outbreaks (He et al., 2019). Under these combined constraints, reliance on a single control strategy is insufficient to effectively suppress banana Fusarium wilt. Instead, integrated management approaches spanning multiple stages, including resistant cultivar breeding, cultivation management, and end-of-life treatment of agricultural residues, are required. The rapid expansion of banana cultivation has generated large quantities of agricultural residues, particularly banana straw, which is typically discarded after harvest (Karim et al., 2015). If improperly managed, these residues can serve as reservoirs for pathogen survival and potential sources of reinfection. Previous studies have shown that high-temperature pyrolysis can effectively inactivate a broad range of plant pathogens, while biochar derived from banana straw exhibits strong adsorption capacity for heavy metals, such as cadmium, in aquatic environments.

Beyond residue sanitization, the functional performance of banana straw–derived biochar is primarily governed by its pore structure, which regulates mass transfer, adsorption behavior, and surface reactivity (Somboon et al., 2025; Yang et al., 2024; Mian et al., 2023). From a pyrolysis perspective, pore formation in biochar is a complex physicochemical process involving the thermal decomposition of biomass components, the progressive construction of the carbon skeleton, and the continuous release and migration of volatile matter (Wang et al., 2025b; Zhylina et al., 2025; Lu and Zong, 2018). In previous studies, biochar pores have generally been classified using two main approaches. One approach distinguishes pores based on their connectivity to the external surface, categorizing them as open or closed pores, while the other classifies pores according to size, including micropores (< 2 nm), mesopores (2–50 nm), and macropores (> 50 nm) (Gao et al., 2020; Sing et al., 1985). Although widely adopted, these classification schemes mainly emphasize geometric or physical attributes and are largely descriptive, which limits their ability to capture the diversity of pore morphologies and the underlying evolutionary mechanisms during biomass pyrolysis and chemical activation.

To overcome this limitation, this study combined SEM-EDS characterization with pore structure analysis to track the structural evolution during the transformation of banana straw into porous biochar under thermochemical coupled activation conditions. The results indicate that the pore structure of the biochar can be classified into four types, including biogenic pores directly inherited from the anatomical structure of banana straw (Pore I), as well as thermochemically derived pores (Pore II, III, and IV) that gradually develop during pyrolysis and subsequent chemical activation. Specifically, Category I pores exhibit higher circularity and lower aspect ratio, reflecting their origin from the native anatomical structure of the biomass and thus their relatively regular geometry (Fig. 5A). Correspondingly, this stage shows the lowest pore density (5458 mm^{-2}) but the highest porosity (60.44%) (Table 4). This suggests that the pore structure at this stage is dominated by large-scale pores, where individual pores contribute substantially to the total pore volume; therefore, despite the limited number of pores, they still account for a high overall porosity.

As pyrolysis proceeds, the Category II pores show a decrease in circularity, while the distribution of aspect ratio becomes significantly broader (Fig. 5B), indicating layered structural breakdown and tensile deformation induced by volatile release and the action of inherent minerals. Correspondingly, the pore density increases markedly to 3.50×10^5 mm^{-2}, whereas the porosity decreases to 37.74% (Table 4). This change suggests that although the number of pores increases, the overall pore size decreases, leading to a reduced contribution of individual pores to the total pore volume and thus a decline in porosity.

In the Category III pore structure formed under KOH activation, circularity increases significantly and the aspect ratio distribution becomes more concentrated, indicating a trend toward more regular pore geometries (Fig. 5C). At this stage, pores are mainly generated by localized etching effects and exhibit relatively uniform hemispherical morphologies. As shown in Table 4, the pore density further increases to 3.08×10^6 mm^{-2}, while the porosity reaches its minimum value (20.59%). This indicates that the pore structure has evolved into a system dominated by a large number of small-scale pores. Despite the substantial increase in pore number, their limited individual volume results in a restricted contribution to the total pore volume, thereby exhibiting a typical "high pore density-low porosity" characteristic.

Further under the synergistic effect of high temperature and intensified chemical activation, the Category IV pore structure tends to stabilize, with circularity and aspect ratio distributions becoming relatively concentrated (Fig. 5D). Notably, although the pore density continues to increase to 4.55×10^6 mm^{-2}, the porosity rises from 20.59% to 23.11%. This is mainly attributed to partial pore expansion and interconnection, which increases the effective pore volume and consequently breaks the previously decreasing trend in porosity.

The BET results and pore size distribution (Table 3) further confirm the evolutionary characteristics of the pore structure at the pore-scale level. As the pyrolysis temperature increases from 500 °C to 800 °C, the micropore volume fraction rises from 8.3% to 64.1%, while the mesopore volume fraction decreases from 91.1% to 35.9%, indicating a gradual transition from a mesopore-dominated structure to a micropore-dominated system. Meanwhile, under the same carbonization

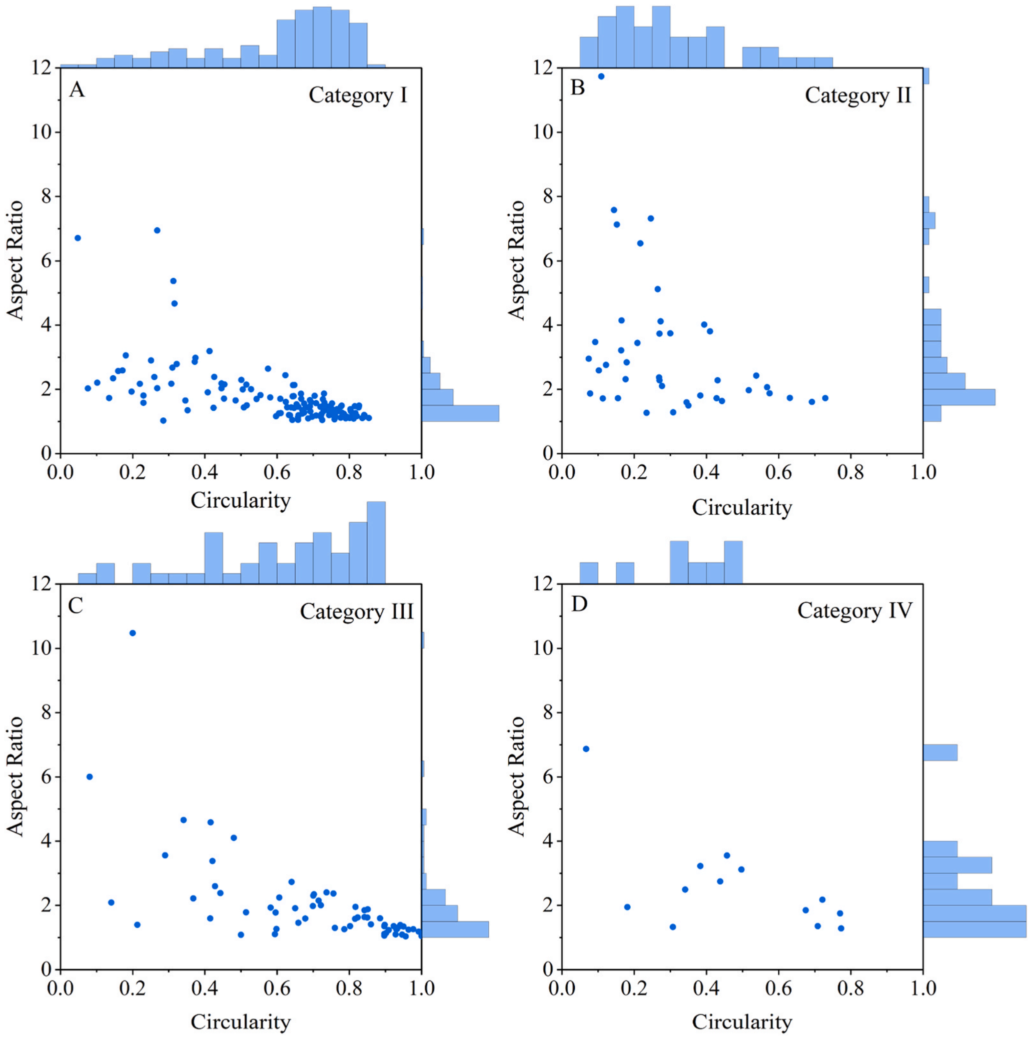

Fig. 5. Two-dimensional morphological feature distributions of pores in banana straw biochar at different evolutionary stages. (A-D) correspond to marginal scatter plots of circularity and aspect ratio for Category I to Category IV pores, respectively.

Table 4
Quantitative morphological characteristics (pore density and porosity) of the four categories of biochar pores.

Pore classification	Pore density（mm^{-2}）	Porosity (%)
Category I	5458	60.44
Category II	349600	37.741
Category III	3874500	16.85
Category VI	4547200	23.105

temperature, increasing KOH dosage further promotes micropore development, suggesting that chemical activation effectively enhances the etching of the carbon framework and facilitates pore wall fragmentation and micropore generation. Mesopores mainly serve as transitional structures during the conversion from macropores to micropores, reflecting an intermediate stage of progressive pore shrinkage. In contrast, the continuous formation and accumulation of micropores are the primary contributors to the increase in specific surface area and pore volume.

Based on the above results, this study constructed a distribution diagram (Fig. 6) using pore density as the x-axis and mean circularity as the y-axis to clearly distinguish pore types. The results show that the four types of pores exhibit distinctly separated distributions within this morphological parameter space, demonstrating good discriminability. Specifically, Category I pores are mainly located in the region of low pore density and high circularity; Category II pores fall within the region

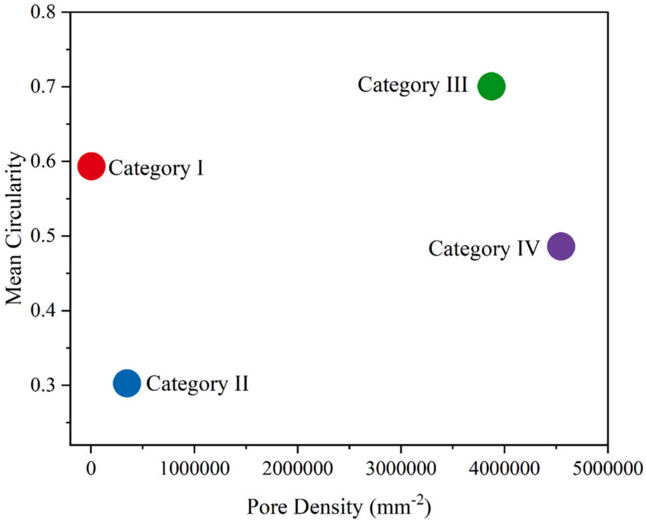

Fig. 6. Distribution characteristics of the four pore categories in the two-dimensional morphological space defined by pore density and mean circularity.

of low circularity and medium pore density; Category III pores are distributed in the region of high pore density and high circularity; and Category IV pores are situated in the region of high pore density and medium circularity. The independent distribution domains of different pore types in the parameter space indicate that the combined parameters of pore density and circularity can effectively characterize structural differences, providing a reliable basis for pore type identification.

In addition, to quantitatively evaluate the effects of pyrolysis temperature (T) and KOH activation concentration (C) on pore structure development, a regression analysis was performed based on the experimental data in Table 3. Considering that linear models are insufficient to capture the nonlinear variations of the parameters, a second-order polynomial response surface model was established. The model incorporated quadratic terms (T^2, C^2) and an interaction term ($T \times C$). Through multiple regression analysis, empirical predictive equations for specific surface area (S_{BET}) and total pore volume (PV) were derived as follows:

$$S_{BET} = -224.54 + 561.31\,C + 0.000986T^2 - 119.44C^2 - 0.0205TC \quad (R^2 = 0.997)$$

$$PV = -0.078 + 0.265\,C + 4.46 \times 10^{-7}T^2 - 0.0757C^2 + 0.00007TC \quad (R^2 = 0.996)$$

The model exhibits high fitting accuracy within the studied range. As an empirical model developed based on experimental data, it can be used to estimate the specific surface area and pore volume of biochar within the defined conditions ($T = 500–800$ °C, $C = 0–1.5$ M), thereby providing a useful reference for experimental parameter optimization and result prediction.

From a broader perspective of research and application, banana straw biochar shows significant potential in adsorption, soil amendment, and carbon sequestration. In terms of functional applications, a well-developed pore structure increases the specific surface area and the number of active sites, thereby enhancing its adsorption capacity for pollutants. Meanwhile, an appropriate porous architecture can also improve soil aeration and water retention, supporting its application in soil remediation. From an ecological perspective, the stability of biochar as a carbon sink is primarily determined by its carbon structural characteristics. Previous studies have shown that highly aromatic and structurally stable carbon in biochar can persist in soils over long periods, thereby acting as an effective carbon sink and contributing to climate change mitigation (Biswal and Balasubramanian, 2025; Enebe et al., 2025). In general, lower H/C and O/C ratios correspond to a higher degree of aromaticity and a lower level of oxidation, respectively, indicating a more stable carbon structure that is more favorable for long-term carbon sequestration. As shown in Table 1, the unactivated sample BSBC500 exhibits the lowest H/C ratio (0.40) and O/C ratio (0.23), indicating a higher degree of aromaticity and stronger structural stability. Therefore, it shows the greatest carbon sequestration potential among all samples. In contrast, with increasing KOH dosage, although the pore structure is significantly enhanced, the O/C ratio increases markedly (up to 0.78), indicating an increase in oxygen-containing functional groups and a more reactive carbon structure. This transformation is beneficial for improving adsorption performance and surface reactivity. At 800 °C, both H/C and O/C ratios increase substantially across all samples (with H/C up to 1.24 and O/C up to 1.91), suggesting that under high temperature and strong chemical activation, the carbon framework undergoes more intense etching and reconstruction, leading to a higher degree of structural disorder. Although such structural features favor pore formation and functional applications, they are unfavorable for long-term carbon stability. Overall, low-temperature and unactivated or mildly activated biochar (e.g., BSBC500) exhibits higher structural stability and is more suitable for long-term carbon sequestration, whereas high-temperature and strongly activated samples, due to their well-developed pore structures and higher surface reactivity, are more suitable for adsorption and environmental remediation applications.

Given the inherently high moisture content of banana straw, future studies may also explore the production of hydrochar via hydrothermal carbonization without complete drying pretreatment (Jelena et al., 2024; Wang et al., 2018). Existing research suggests that hydrothermal carbonization is particularly suitable for high-moisture biomass feedstocks, enabling efficient carbon conversion under relatively mild reaction conditions and demonstrating promising potential for soil conditioning and crop production (Wang et al., 2025c; Yan et al., 2024). However, the practical implementation of thermochemical conversion technologies for banana straw may be constrained by regional variability in production infrastructure, energy availability, and waste management systems. In major banana-producing regions, especially in developing or remote areas, limitations in processing facilities, transportation networks, and energy supply could increase operational costs and hinder large-scale deployment. Moreover, the environmental footprint associated with equipment manufacturing, energy consumption, and by-product management may vary substantially across regions, potentially offsetting some environmental benefits if not properly addressed. Therefore, region-specific assessments integrating feedstock availability, processing conditions, economic costs, and environmental impacts are essential for evaluating the feasibility and sustainability of different thermochemical conversion pathways for banana straw.

5. Conclusion

In this study, banana straw, an abundant industrial crop residue, was successfully converted into hierarchical porous biochar, and the mechanisms underlying pore formation were systematically elucidated. Based on pore morphology, the pores in banana straw biochar were classified into four categories. Category I pores retained the anatomical features of the original biomass (low pore density and high circularity), whereas Category II pores developed as multilayer structures promoted by intrinsic mineral composition and elevated pyrolysis temperature (low circularity and medium pore density). Category III pores, characterized by hemispherical concavities, were induced by KOH activation and became more pronounced with increasing alkaline concentration (high pore density and high circularity). Category IV pores consisted of an interconnected pore network formed through the synergistic effects of high-temperature pyrolysis and intensive KOH impregnation, accompanied by reorganization of the carbon skeleton (high pore density and medium circularity). The composition of the feedstock plays a key regulatory role in pore structure evolution. Si primarily suppresses the reconstruction of the carbon framework through a structural stabilization effect, whereas K promotes the formation and development of pore structures via catalytic activity. In addition, pyrolysis temperature and KOH impregnation intensity significantly regulate pore evolution; with increasing temperature and KOH concentration, carbon framework etching and reconstruction are progressively enhanced, thereby facilitating further pore development. Based on these mechanistic insights, this study further proposes pore structure regulation strategies tailored to different application requirements. For applications that require preservation of the native structure (e.g., microbial carriers), feedstocks with high Si and low K contents combined with mild pyrolysis conditions are recommended. In contrast, for the preparation of high-specific-surface-area materials (e.g., adsorbents or energy storage materials), feedstocks with low Si and high K contents, together with intensified thermochemical coupling, are more suitable. Overall, this study provides a theoretical basis for feedstock selection and pore structure regulation, offering important guidance for the rational design and high-value utilization of biochar materials.

CRediT authorship contribution statement

Chengxiang Gao: Writing-original draft, Investigation, Data curation, and Conceptualization. **Yangzhi Liu**: Writing-original draft, Methodology, and Investigation. **Yuxue Liu:** Writing-review & editing. **Hanjing Xu:** Resources and Data curation. **Lidan Zhang:** Writing-

review & editing. **Junwei Ma**: Writing-review & editing, and Data curation. **Xiaolin Fan:** Writing-review & editing, Supervision, Funding acquisition, Project administration, Conceptualization and Methodology.

Declaration of Competing Interest

The authors declare that they have no known competing financial interests or personal relationships that could have appeared to influence the work reported in this paper.

Acknowledgments

This work was supported by Young Elite Scientists Sponsorship Program by CAST (2023-2025QNRC002), China Agriculture Research System (CARS-31).

Data availability

Data will be made available on request.

References

Acuna, R., Rouard, M., Leiva, A.M., Marques, C., Olortegui, J.A., Ureta, C., Cabrera-Pintado, R.M., Rojas, J.C., Lopez-Alvarez, D., Cenci, A., Cuellar, W.J., Dita, M., 2022. First report of fusarium oxysporum f. Sp. *Cubense* tropical race 4 causing fusarium wilt in cavendish bananas in peru. Plant Dis. 106, 2268. https://doi.org/10.1094/PDIS-09-21-1951-PDN.

Biswal, B.K., Balasubramanian, R., 2025. Use of biomass-derived biochar as a sustainable material for carbon sequestration in soil: recent advancements and future perspectives. Npj Mater. Sustain. 3, 26–27. https://doi.org/10.1038/s44296-025-00066-8.

Bonelli, P.R., Buonomo, E.L., Cukierman, A.L., 2007. Pyrolysis of sugarcane bagasse and co-pyrolysis with an argentinean subbituminous coal. Energy Sources Part a Recovery Util. Environ. Eff. 29, 731–740. https://doi.org/10.1080/00908310500281247.

Brito, M.J.P., Veloso, C.M., Santos, L.S., Bonomo, R.C.F., Fontan, R.D.C.I., 2018. Adsorption of the textile dye dianix® royal blue cc onto carbons obtained from yellow mombin fruit stones and activated with KOH and H_3PO_4: kinetics, adsorption equilibrium and thermodynamic studies. Powder Technol. 339, 334–343. https://doi.org/10.1016/j.powtec.2018.08.017.

Chen, Y., Huang, M., Huang, B., Chen, X., 2012. Mesoporous activated carbon from inherently potassium-rich pokeweed by in situ self-activation and its use for phenol removal. J. Anal. Appl. Pyrolysis 98, 159–165. https://doi.org/10.1016/j.jaap.2012.09.011.

Chen, D., Ju, M., Xie, J., Chen, X., Peng, J., 2024. Current progress on pathogenicity-related genes in fusarium oxysporum f. Sp. *Cubense* tropical race 4. Phytopathol. Res. 6. https://doi.org/10.1186/s42483-024-00274-5.

Cheng, H., Wang, F., Bian, Y., Ji, R., Song, Y., Jiang, X., 2019. Co-and self-activated synthesis of tailored multimodal porous carbons for solid-phase microextraction of chlorobenzenes and polychlorinated biphenyls. J. Chromatogr. A 1585, 1–9. https://doi.org/10.1016/j.chroma.2018.11.047.

Dehkhoda, A.M., Gyenge, E., Ellis, N., 2016. A novel method to tailor the porous structure of KOH-activated biochar and its application in capacitive deionization and energy storage. Biomass. Bioenerg. 87, 107–121. https://doi.org/10.1016/j.biombioe.2016.02.023.

Enebe, M.C., Ray, R.L., Griffin, R.W., 2025. The impacts of biochar on carbon sequestration, soil processes, and microbial communities: a review. Biochar 7, 1–26. https://doi.org/10.1007/s42773-025-00499-3.

Fang, L., Yang, W., Hou, J., Zheng, K., Hussain, A., Zhang, Y., Hou, Z., Wang, X., 2023. Tofukasu-derived biochar with interconnected and hierarchical pores for high efficient removal of Cr(VI). Biochar 5. https://doi.org/10.1007/s42773-023-00268-0.

FAO, 2025. ⟨https://www.fao.org/world-banana-forum/zh/⟩.

Fei, Z., Zibin, P., Fang, W., Suo, C., Rui, C., Jiayu, F., Ping, N., Lijuan, J., 2026. Coffee grounds derived porous nitrogen-rich biochar as a metal-free catalyst for efficient selective oxidation of hydrogen sulfide to sulfur. Biochar 8, 20.

Fu, Y., Shen, Y., Zhang, Z., Ge, X., Chen, M., 2019. Activated bio-chars derived from rice husk via one- and two-step KOH-catalyzed pyrolysis for phenol adsorption. Sci. Total Environ. 646, 1567–1577. https://doi.org/10.1016/j.scitotenv.2018.07.423.

Gan, C., Liu, Y., Tan, X., Wang, S., Zeng, G., Zheng, B., Li, T., Jiang, Z., Liu, W., 2015. Effect of porous zinc–biochar nanocomposites on Cr(VI) adsorption from aqueous solution. Rsc Adv. 5, 35107–35115. https://doi.org/10.1039/C5RA04416B.

Gao, C., Lan, Y., Zhan, Y., Li, Y., Jiang, J., Li, Y., Zhang, L., Fan, X., 2024. Preparation of porous biochar from fusarium wilt-infected banana straw for remediation of cadmium pollution in water bodies. Sci. Rep. 14, 13821. https://doi.org/10.1038/s41598-024-63954-4.

Gao, Y., Yue, Q., Gao, B., Li, A., 2020. Insight into activated carbon from different kinds of chemical activating agents: a review. Sci. Total Environ. 746, 141094. https://doi.org/10.1016/j.scitotenv.2020.141094.

Guo, J., Chen, B., 2014. Insights on the molecular mechanism for the recalcitrance of biochars: interactive effects of carbon and silicon components. Environ. Sci. Technol. 48, 9103–9112. https://doi.org/10.1021/es405647e.

He, J., Zhang, D., Han, M., Liu, X., Wang, Y., Li, Y., Zhang, X., Wang, K., Feng, H., Wang, Y., 2019. One-step large-scale fabrication of nitrogen doped microporous carbon by self-activation of biomass for supercapacitors application. J. Energy Storage 21, 94–104. https://doi.org/10.1016/j.est.2018.11.015.

Herath, A., Layne, C.A., Perez, F., Hassan, E.B., Pittman, C.U., Mlsna, T.E., 2021. Koh-activated high surface area douglas fir biochar for adsorbing aqueous Cr(VI), Pb(II) and Cd(II). Chemosphere 269. https://doi.org/10.1016/j.chemosphere.2020.128409.

Herrera, R.M., Hernandez, Y., Magdama, F., Mostert, D., Bothma, S., Salgado, E.M.P., Teran, D., Gonzalez, E., Angulo, R., Angel, L., Rodriguez, Y., Ortega, R., Viljoen, A., Marys, E.E., 2023. First report of fusarium wilt of cavendish bananas caused by fusarium oxysporum f. Sp. *Cubense* tropical race 4 in venezuela. Plant Dis. 107. https://doi.org/10.1094/PDIS-04-23-0781-PDN.

Hunsom, M., Autthanit, C., 2013. Adsorptive purification of crude glycerol by sewage sludge-derived activated carbon prepared by chemical activation with H_3PO_4, K_2CO_3 and KOH. Chem. Eng. J. 229, 334–343. https://doi.org/10.1016/j.cej.2013.05.120.

Jelena, P., Marija, E., Marija, S., Marija, K., Jelena, D., Aleksandar, J., Janković, P.J., 2024. Hydrothermal carbonization of waste biomass: a review of hydrochar preparation and environmental application. Processes 12, 207.

Jing, H., Zheng, D., Du, H., Zhu, H., Chen, M., Zhou, Y., 2026. Cage-like ulva biochar confined synthesis of Fe_3O_4/ZnO heterojunction nanoparticles for synergistic adsorption and photocatalytic degradation of pfoa. Biochar 8, 11–16. https://doi.org/10.1007/s42773-025-00525-4.

Karim, A.A., Kumar, M., Mohapatra, S., Panda, C.R., Singh, A., 2015. Banana peduncle biochar: characteristics and adsorption of hexavalent chromium from aqueous solution. Int. Res. J. Pure Appl. Chem. 7, 1–10.

Koyama, S., Hayashi, H., 2017. Rice yield and soil carbon dynamics over three years of applying rice husk charcoal to an andosol paddy field. Plant. Prod. Sci. 20, 176–182. https://doi.org/10.1080/1343943X.2017.1290506.

Li, Y., Jiang, S., Jiang, J., Gao, C., Qi, X., Zhang, L., Sun, S., Dai, Y., Fan, X., 2022. Synchronized efficacy and mechanism of alkaline fertilizer and biocontrol fungi for fusarium oxysporum f. Sp. *Cubense* tropical race 4. J. Fungi 8, 261. https://doi.org/10.3390/jof8030261.

Liu, Y., Gao, C., Wang, Y., He, L., Lu, H., Yang, S., 2020. Vermiculite modification increases carbon retention and stability of rice straw biochar at different carbonization temperatures. J. Clean. Prod. 254. https://doi.org/10.1016/j.jclepro.2020.120111.

Lu, S., Zong, Y., 2018. Pore structure and environmental serves of biochars derived from different feedstocks and pyrolysis conditions. Environ. Sci. Pollut. Res. 25, 30401–30409. https://doi.org/10.1007/s11356-018-3018-7.

Mandal, S., Mendhe, A.C., Park, T., Lee, H.S., 2026. Temperature-modulated surface features of neem seed biochar for sustainable thermal energy storage applications. Biochar 8, 9–23. https://doi.org/10.1007/s42773-025-00510-x.

Maymon, M., Sela, N., Shpatz, U., Galpaz, N., Freeman, S., 2020. The origin and current situation of fusarium oxysporum f. Sp. *Cubense* tropical race 4 in israel and the middle east. Sci. Rep. 10. https://doi.org/10.1038/s41598-020-58378-9.

Mian, M.M., Ao, W., Deng, S., 2023. Sludge-based biochar adsorbent: pore tuning mechanisms, challenges, and role in carbon sequestration. Biochar 5, 1–23. https://doi.org/10.1007/s42773-023-00288-w.

Murali, S.P., Ramyabharathi, S.A., Syamala, M., Shreedevasena, S., 2021. Emerging threat: In banana (musa spp.) Cultivation by fusarium oxysporum f. Sp. *Cubense* tropical race (TR4)-Mini review. Emerg. Trends Food Nutr. Health 345–352.

Mustafa, A., Saeed, Q., Lu, X., Farooqi, Z.U.R., Arshad, U., Holatko, J., Wei, W., Mahmood, M., Brtnicky, M., Chen, W., Rebi, A., Ali, M.A., Naveed, M., Kucerik, J., Ghafoor, A., 2026. Beyond one-size-fits-all: tailoring engineered biochar for purpose-specific rhizosphere engineering in crop production, protection, and soil remediation. Biochar 8. https://doi.org/10.1007/s42773-025-00521-8.

Niu, J., Shao, R., Liang, J., Dou, M., Li, Z., Huang, Y., Wang, F., 2017. Biomass-derived mesopore-dominant porous carbons with large specific surface area and high defect density as high performance electrode materials for Li-ion batteries and supercapacitors. Nano Energy 36, 322–330. https://doi.org/10.1016/j.nanoen.2017.04.042.

Peng, H., Gao, P., Chu, G., Pan, B., Peng, J., Xing, B., 2017. Enhanced adsorption of Cu(II) and Cd(II) by phosphoric acid-modified biochars. Environ. Pollut. 229, 846–853. https://doi.org/10.1016/j.envpol.2017.07.004.

Qiu, D., Guo, N., Gao, A., Zheng, L., Xu, W., Li, M., Wang, F., Yang, R., 2019. Preparation of oxygen-enriched hierarchically porous carbon by $KMnO_4$ one-pot oxidation and activation: mechanism and capacitive energy storage. Electrochim. Acta 294, 398–405. https://doi.org/10.1016/j.electacta.2018.10.049.

Rafiq, M.K., Bachmann, R.T., Rafiq, M.T., Shang, Z., Joseph, S., Long, R., 2016. Influence of pyrolysis temperature on physico-chemical properties of corn stover (*Zea mays* L.) Biochar and feasibility for carbon capture and energy balance. Plos One 11, e0156894. https://doi.org/10.1371/journal.pone.0156894.

Rana, M.S., Ren, R., Imran, M., Abdellah, Y.A.Y., Chen, H., Deng, S., Li, J., Lin, J., Wang, R., 2025. Mitigating combined internalized toxicity of nanoplastics and cadmium in rice through metabolic and biochemical regulations under supply of biochar biofilters derived from Mikania micrantha. Biochar 7, 25–98. https://doi.org/10.1007/s42773-025-00488-6.

Shaaban, A., Se, S., Dimin, M.F., Juoi, J.M., Mohd Husin, M.H., Mitan, N.M.M., 2014. Influence of heating temperature and holding time on biochars derived from rubber wood sawdust via slow pyrolysis. J. Anal. Appl. Pyrolysis 107, 31–39. https://doi.org/10.1016/j.jaap.2014.01.021.

Sing, K.S.W., Everett, D.H., Haul, R.A.W., Moscou, L., Pierotti, R.A., Rouquerol, J., Siemieniewska, T., 1985. Reporting physisorption data for gas/solid systems with special reference to the determination of surface area and porosity. Pure. Appl. Chem. 57, 603–619.

Somboon, S., Schlichenmaier, S., Thumanu, K., Pakawanit, P., Yodda, S., Sukitprapanon, T., Lawongsa, P., 2025. Transformations in physicochemical properties and pore structure of biochar derived from rice straw revealed by synchrotron techniques. Sci. Rep. 15. https://doi.org/10.1038/s41598-025-08772-y.

Stokstad, E., 2019. Devastating banana disease may have reached latin america, could drive up global prices. Science. https://doi.org/10.1126/science.aay7681.

Tan, Z., Lu, T., Jerzak, W., Huang, H., Liu, D., Xie, X., Zhang, Q., Ma, Z., Wang, M., Liu, W., Zhang, S., Yang, H., Li, B., 2026. Effects of intrinsic and external potassium on biochar structure evolution in volatile-char interactions during biomass pyrolysis. J. Anal. Appl. Pyrolysis 93, 107472. https://doi.org/10.1016/j.jaap.2025.107472.

Wang, X., Duo, J., Jin, Z., Yang, F., Lai, T., Collins, E., 2025c. Effects of hydrothermal carbonization conditions on the characteristics of hydrochar and its application as a soil amendment: a review. Agronomy 15, 327. https://doi.org/10.3390/agronomy15020327.

Wang, L., Joseph, S., Feng, W., Ye, Y., Zhang, R., Zhang, W., Ning, J., Yang, G., Gao, J., Quan, X., Yu, H., Zhou, X., 2025a. The performance, pyrolysis mechanism and environmental functions of forest surface fuel biochar. Commun. Earth Environ. 6. https://doi.org/10.1038/s43247-025-03016-3.

Wang, W., Wan, W., Chen, Q., Wei, T., Zhang, H., 2024. Banana bunchy top virus movement protein induces resistance in banana against fusarium wilt. Phytopathol. Res. 6. https://doi.org/10.1186/s42483-024-00242-z.

Wang, N., Wang, B., Wang, H., Wu, P., Hassan, M., Wang, S., Zhang, X., 2025b, Engineered biochar for simultaneous removal of heavy metals and organic pollutants from wastewater. Biochar X, e008.

Wang, T., Zhai, Y., Zhu, Y., Li, C., Zeng, G., 2018. A review of the hydrothermal carbonization of biomass waste for hydrochar formation: process conditions, fundamentals, and physicochemical properties. Renew. Sust. Energ. Rev. 90, 223–247. https://doi.org/10.1016/j.rser.2018.03.071.

Xiao, X., Chen, B., Zhu, L., 2014. Transformation, morphology, and dissolution of silicon and carbon in rice straw-derived biochars under different pyrolytic temperatures. Environ. Sci. Technol. 48, 3411–3419. https://doi.org/10.1021/es405676h.

Yan, X., Wang, Z., Zhao, M., Hao, J., Liu, J., Yan, Y., Sun, P., Jia, Y., Ge, G., 2024. Hydrothermal biochar enhances the photosynthetic efficiency and yield of alfalfa by optimizing soil chemical properties and stimulating the activity of microbial communities. Sci. Rep. 14, 31414–31420. https://doi.org/10.1038/s41598-024-83098-9.

Yang, L., Li, S., Ahmed, W., Jiang, T., Mei, F., Hu, X., Liu, W., Abbas, F.M., Xue, R., Peng, X., Zhao, Z., 2024. Exploring the relationship between biochar pore structure and microbial community composition in promoting tobacco growth. Plants-Basel 13. https://doi.org/10.3390/plants13212952.

Yu, L., Yu, M., Lu, X., Tang, C., Liu, X., Brookes, P.C., Xu, J., 2018. Combined application of biochar and nitrogen fertilizer benefits nitrogen retention in the rhizosphere of soybean by increasing microbial biomass but not altering microbial community structure. Sci. Total Environ. 640-641, 1221–1230. https://doi.org/10.1016/j.scitotenv.2018.06.018.

Zeng, G., Zhou, B., Yi, L., Li, H., Hu, X., Li, Y., 2018. Green and facile fabrication of hierarchical N-doped porous carbon from water hyacinths for high performance lithium/sodium ion batteries. Sustain. Energ. Fuels 2, 855–861. https://doi.org/10.1039/c7se00517b.

Zhang, J., Ge, L., Zhang, X., Wang, C., Sun, H., Chen, H., Huang, J., Zhou, S., 2025. A valorization analysis towards agricultural application of biochar prepared using maize straw grown using organic or chemical fertilizers. Sci. Rep. 15, 11413–11469. https://doi.org/10.1038/s41598-025-96258-2.

Zhang, Y., Song, X., Xu, Y., Shen, H., Kong, X., Xu, H., 2019. Utilization of wheat bran for producing activated carbon with high specific surface area via NaOH activation using industrial furnace. J. Clean. Prod. 210, 366–375. https://doi.org/10.1016/j.jclepro.2018.11.041.

Zhao, Q., Meng, Y., Li, J., Xiao, D., 2019a. Sulfur and nitrogen dual-doped porous carbon nanosheet anode for sodium ion storage with a self-template and self-porogen method. Appl. Surf. Sci. 481, 473–483. https://doi.org/10.1016/j.apsusc.2019.03.143.

Zhao, Z., Nie, T., Zhou, W., 2019b. Enhanced biochar stabilities and adsorption properties for tetracycline by synthesizing silica-composited biochar. Environ. Pollut. 254. https://doi.org/10.1016/j.envpol.2019.113015.

Zheng, X., Zhang, D., Wang, F., Yang, X., Wang, X., Chou, S., Xu, P., Yi, W., 2024. Comparison study on silicon forms and leaching characteristics of pyrolysis biochar and hydrochar derived from cow dung digestate. Synth. silica Silicon rice husk Feedstock J. Anal. Appl. Pyrolysis 183, 106846. https://doi.org/10.1016/j.jaap.2024.106846.

Zhylina, M., Miroshnichenko, D., Melnykov, A., Stepanova, V., Lazdovica, K., Zemcenkovs, V., Sterna, V., Ozolins, J., 2025. Biochar structure development during slow pyrolysis of pellets from barley straw and bran. Sci. Rep. 15. https://doi.org/10.1038/s41598-025-26737-z.